# Levitation of a cylinder by a thin viscous film

**Mohit P. Dalwadi**[1]†**, Radu Cimpeanu**[1,2,3]**, Hilary Ockendon**[1]**,
John Ockendon**[1]**, and Tom Mullin**[1,4]

[1]Mathematical Institute, University of Oxford, Oxford OX2 6GG, UK
[2]Mathematical Institute, Zeeman Building, University of Warwick, Coventry CV4 7AL, UK
[3]Department of Mathematics, Imperial College London, London SW7 2AZ, UK
[4]Linacre College, University of Oxford, Oxford OX1 3JA, UK

When a horizontal cylinder is placed on a vertically moving belt coated with a thin layer of viscous fluid, experiments reveal that, at a specific belt velocity, the cylinder can be levitated at a fixed height while rotating around its own axis at an *a priori* unknown rate. We develop and solve a model for this experiment, using a combination of asymptotic analysis and direct numerical simulation. We obtain a relationship between belt speed and cylinder rotation rate which we successfully compare with experimental results.

## 1. Introduction

A vertical wall is covered in a thin layer of oil that is sufficiently viscous for drainage effects to be negligible. When a cylinder is placed on the wall with its axis horizontal, it will roll down the wall. However, if the wall is translated upwards, is it possible to keep the centre of the cylinder fixed in place in the laboratory frame by adjusting the speed of the wall? In this paper we will address this question, which is an example of steady levitation by a viscous fluid.

Levitation of solids and liquids by acoustic or magnetic forces is a well-studied area, but levitation by hydrodynamic forces has received less attention. Thin film levitation has been studied by, for example, Fitt *et al.* (2004); Hinch & Lemaitre (1994); Lhuissier *et al.* (2013); de Maleprade *et al.* (2018); and Sawaguchi *et al.* (2019). All these papers consider different configurations from the one considered here. Our work builds on the studies of levitation by vertical belts initiated by Eggers *et al.* (2013) for a cylinder and by Mullin *et al.* (2020) for a block. Although our work has been driven by scientific curiosity, we will find that it has relevance to practical problems such as the lubrication of bearings and coating flows.

We carry out a theoretical and experimental investigation of a rigid circular cylinder placed horizontally on a vertical belt moving upwards and covered by a thin layer of oil. A schematic of the experiment is shown in figure 1. We are interested in the case in which the cylinder centre remains at a fixed position in the laboratory frame with an appropriate choice of the belt speed. As the belt moves upwards, the cylinder rotates about its own axis at a rate that is lower than the associated slip velocity induced by

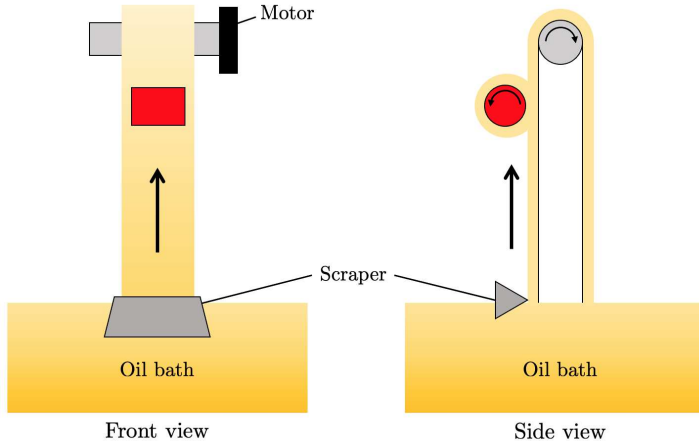† Email address for correspondence: dalwadi@maths.ox.ac.uk

Figure 1: Schematic diagram of the experimental apparatus showing a cylinder balanced on the belt, which is covered in a layer of oil. Videos of this experiment are provided as supplementary material.

the belt. Rotation also occurs in the problem of a sphere travelling down an inclined plane covered with a thin viscous film, which was investigated in Bico *et al.* (2009). The geometry of our experiment is similar to those in coating flows, see for example Duffy & Wilson (1999); Ruschak (1985); and Weinstein & Ruschak (2004), and this experiment is also related to the film splitting flow described by Coyle *et al.* (1986).

The experimental setup we consider has been modelled previously by Eggers *et al.* (2013) within a lubrication framework. While successful in determining the qualitative relationship between cylinder rotation rate and belt speed required for levitation, their model did not account for the flow travelling around the cylinder, nor the coalescence/separation flow regions at the inlet/outlet to the lubrication region, and their theoretical results did not agree quantitatively with the experimental data presented therein. This motivates a more comprehensive approach detailed in the present work, in which we specifically account for the fluid travelling around the cylinder and investigate the important inner problem for the full system. These differences lead to different solutions from those in Eggers *et al.* (2013), and mean that we are able to formally close the complex mathematical system. Our solutions show good agreement with the experimental data. Moreover, we are able to shed light on the onset of fluid tongues in the experiment.

There are several crucial distinctions between levitating a cylinder, which we investigate here, and levitating a block, which was considered in Mullin *et al.* (2020). Most obviously, with a cylinder, the downstream fluid forms a coating flow around the top of the cylinder, and rejoins with the fluid upstream of the cylinder, as shown in figure 1. With a block, the fluid passes between the block and the belt, and the top side of the block remains dry. Additionally, the cylinder rotates about its own axis while a block does not. Moreover, in the case of a cylinder, it is observed that there is a unique belt speed that levitates the cylinder. This is different to the case of a block levitating on a thin viscous film, where a continuum of belt speeds resulting in levitation is possible for a given block. In addition, a block has two degrees of freedom in its position - the height of its midpoint from the belt, and the angle it makes with the belt. The cylinder loses a degree of freedom related to an angle, but gains a degree of freedom in its rotation
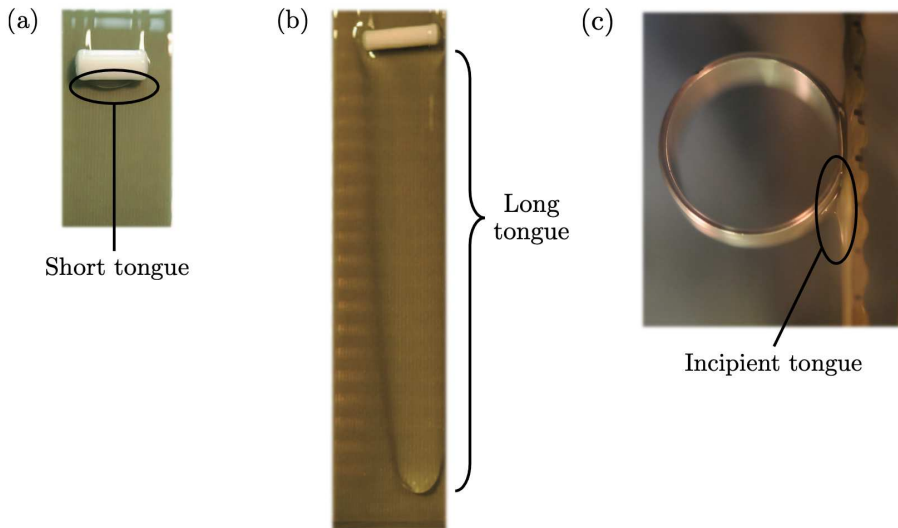
Figure 2: Tongues arising from cylinder levitation on 0.3 mm layers of silicone oil. (a) 12mm long, 5 mm diameter PTFE cylinder, exhibiting a short tongue. (b) 12 mm long, 4 mm diameter PTFE cylinder, exhibiting a long tongue. (c) 15 mm long, 8 mm diameter hollow aluminium cylinder, exhibiting an incipient tongue.

rate. Moreover, the position of the air–oil free surface relative to the lubrication region underneath the block is known *a priori* - it is located at the ends of the block. However, this is not the case with a cylinder. The positions of the inlet and outlet terminating menisci must be determined as part of the solution, adding two additional degrees of freedom to the system.

In the block levitation considered in Mullin *et al.* (2020), there was usually a fluid tongue that propagated downwards at a uniform speed from the corner of the block. This meant there was no steady state in the system and so the fluid flux leaving the system downstream of the block was not equal to the flux entering the system far upstream of the tongue. The presence of a tongue is fundamental to the ability of a block to levitate on a moving belt. The action of the tongue is different in the case of a cylinder, where one of two types of tongue behaviour is possible; both are shown in figure 2. In the first type the tongue is very small and does not grow with time. The experimental data in Eggers *et al.* (2013) is all of the first type. In the second type there is a much longer tongue, which grows with a velocity around $20 - 100$ times slower than the belt speed, and the tongue either reaches a fixed length or reaches the bottom of the belt. Tongues do not form for cylinders with larger radii, but as the cylinder radius is decreased there is a critical radius at which a tongue starts to form. After this point, a small decrease in cylinder radius results in a much longer tongue at steady state.

In this paper, we present a steady two-dimensional model for the coupled fluid flow and cylinder motion problem. We analyse this model using a combination of the method of matched asymptotic expansions and direct numerical simulation (DNS), and compare its predictions with the experimental results. While our asymptotic analysis reveals that the majority of the important behaviour occurs within the lubrication region between the belt and cylinder, this region has an *a priori* unknown finite extent. Hence, the end-points of the lubrication region must be determined as part of the solution, resulting in a free boundary problem. To close the asymptotically reduced system we must solve a

non-trivial inner problem near the upper meniscus, which we derive systematically. To solve for the flow in this region, we use a powerful (but expensive) numerical approach, allowing us to efficiently target the use of computational resources to the region that closes the problem. Our strategy ensures we can characterise the flow over a wide range of parameters, while successfully validating our model by comparison to the available experimental data.

The structure of this paper is as follows. We first describe the experiment in §2. We present a dimensional description of a model that neglects gravitational forces in the liquid in §3, which we subsequently nondimensionalise. We solve this system in §4, using a combination of asymptotic and numerical techniques, and validate our results against the experimental data. In §5 we briefly assess the importance of gravitational forces in the liquid and the possible occurrence of tongues, before discussing our results and some open questions in §6.

## 2. Experimental set-up

A 375 mm long and 26.5 mm wide steel-reinforced plastic timing belt was driven vertically, as shown in the schematic diagram of the apparatus in figure 1. The outside of the belt provided a smooth moving surface of length 150 mm. The belt was driven by one of a pair of 38 mm toothed pulleys which were matched to the teeth on the inside of the belt. The drive was provided by a DC motor with a controlled feedback loop which was connected to the drive pulley through a 50:1 gearbox. The rotation rate of the drive was measured using a calibrated optical shaft encoder.

The viscous fluid was silicone oil with a measured dynamic viscosity of $\tilde{\mu} = 13341 \pm 50$ cP at 21°C. The experiments were carried out in a controlled environment where the temperature of the oil was measured to be $21 \pm 0.5$°C. The density of the silicone oil was $\tilde{\rho} = 0.971 \pm 0.001$ g cm$^{-3}$ and the oil-air surface tension was $\tilde{\gamma} = 21.5$ mN m$^{-1}$. Silicone oil readily coats and wets the belt, which enabled the formation of a uniform layer. The belt passed through a 2 cm deep bath of oil and the thickness of the layer was set using a knife edge which acted as a scraper fixed at a controlled distance from the belt, which was between 0.1–1 mm. The uniformity and depth of the layer were measured using a commercial confocal optical device from Micro-Epsilon (confocalDT). It was found to be constant to within 10% over the central portion of the belt.

The cylinders were made from polytetrafluoroethylene (PTFE), also known as Teflon, and had a density of $\tilde{\rho}_s = 2.2$ g cm$^{-3}$. The cylinder length was always 12 mm, and the cylinder radius ranged from $\tilde{a} = 2$–8 mm. The belt speed required to levitate these cylinders ranged between $\tilde{U}_b = 1$–35 mm s$^{-1}$. A few experiments on tongue development were performed using plastic printed cylinders. These cylinders had lengths of 12.35 mm, diameters of 5.80 – 7.95 mm, and were printed using the material acrylonitrile butadiene styrene (ABS), which has a density of 1.04 g cm$^{-3}$.

### 2.1. *Experimental protocols*

The apparatus was run for an initial period of 30 minutes to establish a uniform film of viscous fluid on the belt before any levitation experiment was carried out. The thickness of the film was set using the knife edge. Achieving levitation with cylinders was relatively straightforward and involved placing a cylinder on the moving layer and adjusting the speed of the belt to achieve balance. If the belt speed was too high, the cylinder moved up the belt, too low and it travelled down the belt. A given cylinder would always rotate around its own axis at a rate that was found to be independent of the belt speed. A typical set of results illustrating these points are shown in figure 3. It can be seen in
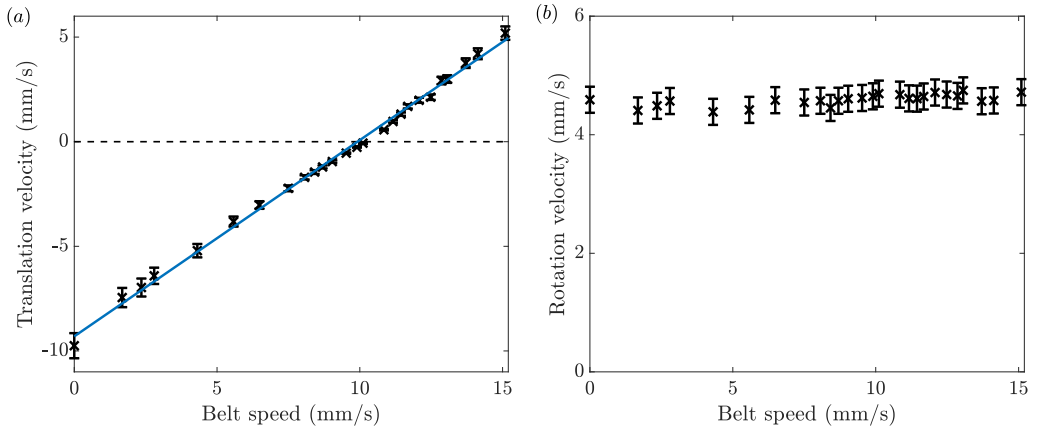
Figure 3: (a) The translation velocity of a cylinder in the laboratory frame. The dashed black line represents a cylinder that is fixed in the laboratory frame, so below/above this line the cylinder moves down/up the belt. The solid blue line shows a linear best fit of the data ($R^2 = 0.997$). (b) The rotation velocity (rotation rate multiplied by cylinder radius) of the same cylinder, which we see is essentially independent of belt speed. For this data we use a 8 mm diameter, 12 mm long PTFE cylinder on a 0.3 mm oil layer. The data are collected by measuring the time taken for the cylinder to translate 100 mm, and averaged over ten repetitions. The error bars correspond to one standard deviation of the data.

figure 3a that there is a linear relationship between the belt speed and the cylinder translation velocity, and that the translation speed is zero for a particular belt speed *i.e.* the cylinder is balanced at a unique belt speed. The gradient of this linear relationship is approximately 1. This is because the problem of determining the belt speed required for levitation is equivalent to determining the cylinder fall speed with a stationary belt for the following reason. The cylinder translates at an approximately uniform speed, since inertial terms are small, and so the frame moving with the cylinder is inertial. At this specific belt speed, the cylinder centre is stationary in the laboratory frame while the cylinder continues to rotate about its own axis. This balance was observed to be stable over a timescale of at least 12 hours. Note that the balance speed and cylinder rotation rate were dependent on the size and weight of cylinder used. Occasionally, a mild rippling in the free surface is observed downstream of the cylinder, analogous to the classic printer's instability (Pearson 1960), but this does not appear to affect the cylinder motion.

The majority of the experiments were performed with cylinders with radii which were larger than the layer thickness by a factor of approximately 10. In these cases a small stable tongue was observed to form on the upstream side of the cylinder as in figure 2(a). For smaller cylinders, the tongue could grow to much longer lengths, as shown in figure 2(b). Part of our modelling work will involve understanding the onset of tongue formation. We will consider a two-dimensional model of the fluid problem, neglecting any edge effects near the ends of the cylinder (e.g. deformations in the fluid surface near the ends of the cylinder in figure 2). Even with these assumptions, the model predicts results that agree well with experimental data.
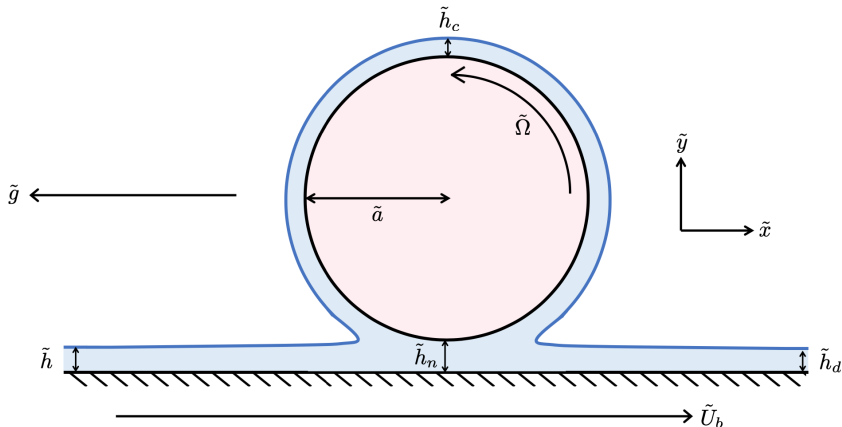
Figure 4: Schematic of the model we consider in this paper. The lower (hashed) black line denotes the belt, the circle denotes the cylinder, and the blue line denotes the fluid free surface. For lighter cylinders, a tongue may form at the left meniscus.

## 3. Mathematical model

We model the steady state of the experiment described in §2. We consider the motion of a rigid circular cylinder which sits on a thin layer of oil covering a moving wall. We consider a two-dimensional cross-section of the cylinder, with coordinate system $(\tilde{x}, \tilde{y})$ centred on the belt at the closest point to the cylinder, *i.e.* the nip point, aligned such that the positive $\tilde{x}$-axis is in the direction of the moving belt and the positive $\tilde{y}$-axis points from belt to cylinder. We use tildes to denote dimensional quantities throughout. We will model the flow of the viscous fluid and the position of its free surface, and couple this to the motion of the cylinder, each of which must be determined as part of the solution. The fluid velocity is denoted as $\tilde{\boldsymbol{u}} = \tilde{u}\boldsymbol{e}_{\tilde{x}} + \tilde{v}\boldsymbol{e}_{\tilde{y}}$, where $\boldsymbol{e}_{\tilde{x}}$ and $\boldsymbol{e}_{\tilde{y}}$ are the unit vectors in the $\tilde{x}$ and $\tilde{y}$-directions, respectively, and the fluid pressure is denoted as $\tilde{p}$. We provide a schematic of the model setup in figure 4.

Since the Reynolds number based on a typical cylinder radius and belt speed is of $O(10^{-3})$, the dimensional governing equations within the fluid are the incompressible steady Stokes flow equations

$$\tilde{\nabla}\tilde{p} = \tilde{\mu}\tilde{\nabla}^2\tilde{\boldsymbol{u}} - \tilde{\rho}\tilde{g}\boldsymbol{e}_{\tilde{x}}, \quad \tilde{\nabla} \cdot \tilde{\boldsymbol{u}} = 0, \qquad (3.1)$$

where the (constant) parameters are the fluid dynamic viscosity $\tilde{\mu}$, the fluid density $\tilde{\rho}$, and the acceleration due to gravity $\tilde{g}$.

At the solid boundaries, the fluid satisfies the no-slip condition. Therefore, on the belt we impose the boundary condition

$$\tilde{\boldsymbol{u}} = \tilde{U}_b\boldsymbol{e}_{\tilde{x}}, \qquad (3.2a)$$

where $\tilde{U}_b$ is the *a priori* unknown belt velocity, and on the cylinder surface we impose

$$\tilde{\boldsymbol{u}} = \tilde{a}\tilde{\Omega}\boldsymbol{t}, \qquad (3.2b)$$

where $\tilde{a}$ is the cylinder radius, and $\tilde{\Omega}$ is the *a priori* unknown angular velocity of the cylinder. Here, $\boldsymbol{t}$ is the unit vector tangent to the cylinder surface in the anti-clockwise direction.

At the free fluid-air boundary, the normal stress is balanced by surface tension, and

the tangential stress vanishes, yielding

$$\tilde{\sigma} \cdot \boldsymbol{n} = \tilde{\gamma} \left( \tilde{\nabla} \cdot \boldsymbol{n} \right) \boldsymbol{n}, \tag{3.3}$$

where $\tilde{\sigma}$ is the stress tensor of the fluid, $\tilde{\gamma}$ is the (constant) fluid-air surface tension, and $\boldsymbol{n}$ points out of the fluid.

Far upstream, the film thickness is prescribed and the free surface, described by $\tilde{y} = \tilde{H}(\tilde{x})$, satisfies

$$\tilde{H} \to \tilde{h} \quad \text{as } \tilde{x} \to -\infty, \tag{3.4a}$$

where $\tilde{h}$ is the imposed upstream film thickness. Far downstream, the film thickness is uniform and the free surface satisfies

$$\frac{\mathrm{d}\tilde{H}}{\mathrm{d}\tilde{x}} \to 0 \quad \text{as } \tilde{x} \to \infty. \tag{3.4b}$$

The force and torque acting on the cylinder result from gravity and the fluid stress. Since we are considering a cylinder whose centre is fixed in the laboratory frame, the dimensional force balance is

$$\pi \tilde{a}^2 \tilde{\rho}_s \tilde{g} \boldsymbol{e}_{\tilde{x}} = \oint_{\partial \tilde{S}} \tilde{\sigma} \cdot \boldsymbol{n} \, \mathrm{d}\tilde{S}, \tag{3.5}$$

where $\pi \tilde{a}^2 \tilde{\rho}_s$ is the mass of the cylinder per unit length, $\tilde{\rho}_s$ is the cylinder density, and $\partial \tilde{S}$ is the surface of the two-dimensional cross-section of the cylinder. In a similar manner, the dimensional torque balance yields

$$\oint_{\partial \tilde{S}} \tilde{\boldsymbol{r}} \times (\tilde{\sigma} \cdot \boldsymbol{n}) \, \mathrm{d}\tilde{S} = \boldsymbol{0}, \tag{3.6}$$

where $\tilde{\boldsymbol{r}}$ is the position vector of a point on the surface of the cylinder with respect to the centre of the cylinder.

The experimental parameter values are given in §2, and summarised for convenience in Table 1. At this point we emphasise that the belt speed $\tilde{U}_b$ and the cylinder rotation rate $\tilde{\Omega}$ are initially unknown for a given cylinder, and must be determined as a function of the remaining system parameters. Moreover, of the various parameters to be calculated as part of the solution, $\tilde{U}_b$ and $\tilde{\Omega}$ are the most easily measurable experimental quantities; they will serve as helpful quantities with which to validate our model.

### 3.1. *Asymptotic structure*

Since the ratio $\tilde{h}/\tilde{a} =: \epsilon$ is small, we expect to be able to model much of the flow by lubrication theory. However, before we nondimensionalise the system, it is helpful to understand the asymptotic regions present in the flow problem in the limit $\epsilon \to 0$, in order to focus on the most important regions. As such, we now outline the asymptotic structure of the dimensionless problem with lengths scaled with cylinder radius.

In the limit $\epsilon \to 0$, there are six asymptotic regions in the system, as illustrated in figure 5. The first region (Region I) is the thin layer of oil between the scraper at the bottom of the belt and the tip of any tongue created by the cylinder. Scaling length with cylinder radius, it has thickness $\epsilon$ and length of $O(1)$. In this region the fluid from the scraper is undisturbed - the fluid moves up the belt with a free surface parallel to the belt.

Region II is the small upstream coalescence region representing the inlet of the nip region between the belt and the cylinder. The flow is two-dimensional here and so, in the

| Dimensional parameter | Description | Value | Units |
|:---:|:---:|:---:|:---:|
| $\tilde{\rho}$ | Fluid density | $0.971 \times 10^3$ | kg m$^{-3}$ |
| $\tilde{\rho}_s$ | Cylinder density | $2.2 \times 10^3$ | kg m$^{-3}$ |
| $\tilde{\mu}$ | Dynamic viscosity | $1.33 \times 10^1$ | Pa s |
| $\tilde{\gamma}$ | Surface tension | $2.15 \times 10^{-2}$ | N m$^{-1}$ |
| $\tilde{U}_b$ | Belt velocity | $0.1 - 3.5 \times 10^{-2}$ | m s$^{-1}$ |
| $\tilde{h}$ | Film thickness at knife | $1 - 10 \times 10^{-4}$ | m |
| $\tilde{a}$ | Cylinder radius | $2 - 8 \times 10^{-3}$ | m |
| $\tilde{g}$ | Gravity | $9.81$ | m s$^{-2}$ |

| Dimensionless parameter | Definition | Order of magnitude |
|:---:|:---:|:---:|
| $\epsilon$ | $\tilde{h}/\tilde{a}$ | $O(10^{-2} - 10^{-1})$ |
| Re | $\tilde{\rho}\tilde{a}\tilde{U}_b/\tilde{\mu}$ | $O(10^{-3})$ |
| $M$ | $\pi\tilde{\rho}_s\tilde{g}(\tilde{h}\tilde{a}^3)^{1/2}/\tilde{\mu}\tilde{U}$ | $O(1)$ |
| $\Gamma$ | $\tilde{\rho}\tilde{g}(\tilde{h}\tilde{a}^3)^{1/2}/\tilde{\mu}\tilde{U}$ | $O(1)$ |
| Ca | $\tilde{\mu}\tilde{U}/\tilde{\gamma}$ | $O(1 - 10)$ |

Table 1: The experimental parameters referred to in §2, the parameters to which we refer in our mathematical model, and the typical values of each.
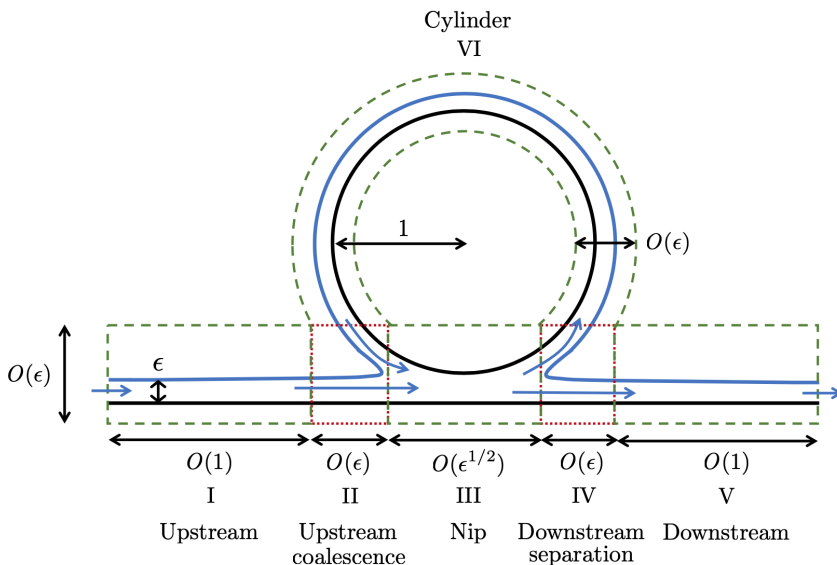


Figure 5: A schematic of the asymptotic regions involved in the dimensionless system, assuming no tongue formation. The regions with boundaries denoted as dashed green lines are lubrication regions and those denoted with dotted red lines are transition regions. All lengths are measured relative to the cylinder radius.

absence of a tongue, its thickness and length are of $O(\epsilon)$. In Region II, the cylinder is physically present in the problem, but its surface appears flat here (not shown in figure 5). This is in contrast to the free surface, whose curvature is apparent at leading order in this region. This inlet region marks the three-way transition between the fluid coming in from over the cylinder (Region VI, discussed below), the fluid entering from upstream (Region I), and the fluid entering the nip region between the belt and the cylinder (Region III, discussed below). The extent of Region II must be determined as part of the solution.

Region III is the thin nip region between the belt and the cylinder. Its thickness is of $O(\epsilon)$ and, since the cylinder cross-section is circular, its length is of $O(\epsilon^{1/2})$. We will find that the leading-order force and torque acting on the cylinder occur in this region. In Region III, the curvature of the cylinder is apparent and is well-approximated by a parabola to leading order. In addition, there is no free surface between the oil and the air in Region III, but the position of the coalescence and separation regions at either end of this region must be determined as part of the solution. Hence, Region III can be characterised as a free-boundary lubrication problem with two unknown end positions.

The small downstream separation region is Region IV. As the flow is fully two-dimensional here, its thickness and length are of $O(\epsilon)$. This marks the outlet of the nip region between the belt and the cylinder. In a similar way to Region II, the cylinder is physically present in this region, though it again appears to be flat since its length is of the same order as the downstream film thickness. The curvature of the free surface is apparent at leading order in Region IV, and this region marks the three-way transition between the fluid leaving the nip from Region III to head downstream of the cylinder (Region V) and to coat the cylinder (Region VI).

Once the fluid leaves the cylinder behind, it enters Region V. This region is the downstream equivalent of Region I. Its thickness is $\epsilon$ and its length is of $O(1)$. In this region the fluid moves downstream with a free surface parallel to the belt, with the same thickness as the free surface in Region I since the system is in a steady state.

The final Region VI corresponds to the fluid travelling over the surface of the cylinder. Its thickness is of $O(\epsilon)$ and its length is of $O(1)$. Here, the fluid moves around the cylinder, transporting fluid from the downstream separation region (IV) to the upstream coalescence region (II).

While the above regions are all coupled to one another, the most important regions to understand levitation are Regions II, III, and IV. While the importance of Region III is fairly intuitive, the importance of Regions II and IV is best demonstrated after investigating Region III. Thus, in the next section we nondimensionalise the system using variables appropriate for Region III.

### 3.2. *Dimensionless system*

We nondimensionalise the system using the scalings outlined for Region III in figure 5, the nip region between belt and cylinder. That is, we use the geometric mean of the upstream film thickness $\tilde{h}$ and the cylinder radius $\tilde{a}$ as the $\tilde{x}$-direction lengthscale and the upstream film thickness as the $\tilde{y}$-direction lengthscale. In addition, we use a typical belt speed to scale the $\tilde{x}$-direction velocity, and use a $\tilde{y}$-direction velocity scaling that achieves a balance in the lubrication equations. This results in the scalings

$$\tilde{x} = (\tilde{h}\tilde{a})^{1/2}x, \quad \tilde{y} = \tilde{h}y, \quad \tilde{u} = \tilde{U}u, \quad \tilde{v} = \epsilon^{1/2}\tilde{U}v, \quad (\tilde{p}, \tilde{\sigma}) = (\tilde{\mu}\tilde{U}/\tilde{a}\epsilon^{3/2})(p, \sigma), \quad (3.7)$$

where $\tilde{U}$ is a typical value of the belt velocity.

Using the scalings (3.7) in the dimensional equations (3.1), we obtain the dimensionless

governing equations

$$p_x = u_{yy} + \epsilon u_{xx} - \epsilon^{3/2}\Gamma, \quad p_y = \epsilon v_{yy} + \epsilon^2 v_{xx}, \quad u_x + v_y = 0, \tag{3.8}$$

where $\Gamma := \tilde{\rho}M/\pi\tilde{\rho}_s$ and $M := \pi\tilde{\rho}_s\tilde{g}(\tilde{h}\tilde{a}^3)^{1/2}/\tilde{\mu}\tilde{U}$ is the dimensionless weight per unit length of the cylinder. In the next section, it will become apparent that the parameter $M \leqslant O(1)$ in order for levitation to occur, and it will henceforth be regarded as a control parameter.

The position of the cylinder is defined by

$$x^2 - 2(y - h_0) + \epsilon(y - h_0)^2 = 0, \tag{3.9}$$

with $h_0 := \tilde{h}_n/\tilde{h}$, where $\tilde{h}_n$ is the nip height as shown in figure 4, and hence $h_0$ is to be determined. On each solid surface, the scaled boundary conditions (3.2) are as follows

$$\boldsymbol{u} = U\boldsymbol{e}_x \quad \text{on the belt,} \qquad \boldsymbol{u} = \Omega\boldsymbol{t} \quad \text{on the cylinder,} \tag{3.10}$$

where $U = \tilde{U}_b/\tilde{U}$ is the unknown dimensionless belt speed and $\Omega = \tilde{a}\tilde{\Omega}/\tilde{U}$ is the unknown dimensionless rotation rate of the cylinder, $\boldsymbol{e}_x$ is the unit vector in the $x$-direction, and $\boldsymbol{t}$ is the unit tangent vector in the anti-clockwise direction.

Scaling $\mathrm{d}\tilde{S}$ with $(\tilde{h}\tilde{a})^{1/2}$ in (3.5), the force balance is

$$\epsilon^{1/2}M\boldsymbol{e}_x = \oint_{\partial S} \sigma \cdot \boldsymbol{n}\,\mathrm{d}S. \tag{3.11}$$

The torque balance (3.6) is simply

$$\oint_{\partial S} \boldsymbol{r} \times (\sigma \cdot \boldsymbol{n})\,\mathrm{d}S = \boldsymbol{e}_z \oint_{\partial S} \boldsymbol{t} \cdot (\sigma \cdot \boldsymbol{n})\,\mathrm{d}S = \boldsymbol{0}. \tag{3.12}$$

In the simplest configuration, we expect the nip region to extend between two free boundaries with Regions II, IV, so that $x_- < x < x_+$ where $x_{\pm}$ must be determined as part of the solution. We will address this free boundary problem in the next section.

## 4. Solving the model

We now investigate the dimensionless system (3.8)–(3.12) by performing an asymptotic analysis to systematically reduce the complexity of the system, exploiting the limit $\epsilon \to 0$. Our analysis starts by exploring the lubrication region III as far as possible, before deriving the appropriate closure conditions by investigating the coalescence and separation regions II and IV, always assuming no significant tongue formation.

### 4.1. *Region III: Nip under cylinder*

In this region, the fluid is enclosed by the cylinder and the belt, and the region terminates in small menisci at each end, corresponding to free boundaries.

Taking the limit $\epsilon \to 0$, the system (3.8) becomes the usual lubrication equations

$$p_x = u_{yy}, \quad p_y = 0, \quad u_x + v_y = 0 \qquad \text{for } x_- < x < x_+, \quad 0 < y < H(x), \tag{4.1}$$

where the dimensionless leading-order cylinder surface is located at $y = H(x)$, where

$$H(x) := h_0 + x^2/2. \tag{4.2}$$

The boundary conditions (3.10) become

$$u = U, \quad v = 0 \quad \text{on } y = 0, \qquad u = \Omega, \quad v = \Omega x \quad \text{on } y = H(x). \tag{4.3}$$

We proceed in the usual manner to deduce

$$u = \frac{p_x}{2} y(y - H) + \frac{y}{H} (\Omega - U) + U. \tag{4.4}$$

We define the unknown flux as

$$Q_c := \int_0^H u \, dy = -\frac{p_x}{12} H^3 + (\Omega + U) \frac{H}{2}. \tag{4.5}$$

Rearranging (4.5) yields the following ODE for the pressure,

$$\frac{dp}{dx} = \frac{6 (U + \Omega)}{H^2} - \frac{12 Q_c}{H^3} \quad \text{for } x_- < x < x_+, \tag{4.6}$$

which can be solved analytically as follows

$$p = 3 \left( U + \Omega - \frac{3 Q_c}{2 h_0} \right) \left( \frac{x}{h_0 H} + \sqrt{2} \frac{\tan^{-1} x/\sqrt{2 h_0}}{h_0^{3/2}} \right) - \frac{3 Q_c x}{h_0 H^2} + P_0, \tag{4.7}$$

where $P_0$ is an unknown constant of integration. Hence, apart from a constant, $p$ is an odd function of $x$.

Finally, we note that the leading-order stress on the cylinder is

$$\sigma \cdot n|_{y=H} = -\epsilon^{1/2} \left( p \frac{dH}{dx} + \frac{\partial u}{\partial y} \right)\Big|_{y=H} e_x + p|_{y=H} \, e_y, \tag{4.8}$$

where

$$\frac{\partial u}{\partial y}\Big|_{y=H} = \frac{2 (U + 2\Omega)}{H} - \frac{6 Q_c}{H^2}. \tag{4.9}$$

Hence, in combination with (3.11), we deduce that $M \leqslant O(1)$ and $\tilde{U}_b = O(\tilde{\rho}_s \tilde{g} (\tilde{h} \tilde{a}^3)^{1/2} / \tilde{\mu})$.

We have now proceeded as far as possible in Region III without invoking any global or matching conditions. At this point it is worth emphasizing the unknowns in the system. They are $\Omega$, $Q_c$, $h_0$, $P_0$, $x_-$, $x_+$, and $U$. To determine these seven unknowns, we need seven equations. Three of these will come from force and torque balances on the cylinder, and the remaining four will come from asymptotic matching with the coalescence and separation regions at either end of Region III. It will soon become apparent that it will suffice to solely consider Region IV, even though the local models for the Regions II and IV are similar. For the moment, we expect the flow pattern in Region IV to be as in figure 6 and a solution for this configuration will be presented in §4.3.

### 4.2. Regions IV: the separation zone

To scale into Region IV, we write

$$x = x_+ + \epsilon^{1/2} H(x_+) X, \quad y = H(x_+) Y, \quad (p, \sigma) = \frac{\epsilon^{1/2}}{H(x_+)} (P, \Sigma), \quad v = V/\epsilon^{1/2}. \tag{4.10}$$

At leading order, the flow is governed by the incompressible Stokes equations

$$\frac{\partial P}{\partial X} = \frac{\partial^2 u}{\partial X^2} + \frac{\partial^2 u}{\partial Y^2}, \quad \frac{\partial P}{\partial Y} = \frac{\partial^2 V}{\partial X^2} + \frac{\partial^2 V}{\partial Y^2}, \quad \frac{\partial u}{\partial X} + \frac{\partial V}{\partial Y} = 0. \tag{4.11}$$

The boundary conditions on the solid surfaces are

$$u = U, \quad V = 0 \quad \text{on } Y = 0, \quad u = \Omega, \quad V = 0 \quad \text{on } Y = 1. \tag{4.12}$$
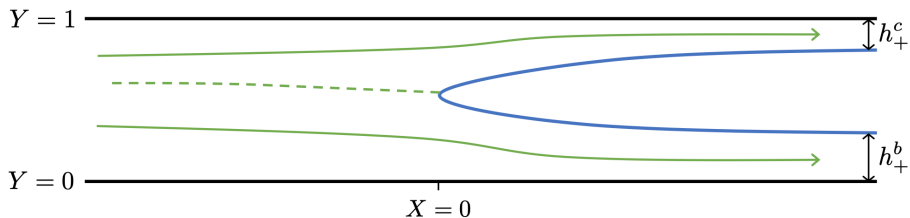
Figure 6: The inner problems for Region IV. The green arrows denote the direction of the flow with dashed line denoting the dividing streamline. The solid black lines are solid boundaries, and the blue curved line denotes the free surface. We note that there may be more than one dividing streamline with accompanying recirculation zones for low capillary numbers (Coyle *et al.* 1986).

On the free surface, surface tension may be important and the dimensional stress condition (3.3) becomes

$$\Sigma \cdot \boldsymbol{n} = \frac{\kappa}{\text{Ca}} \boldsymbol{n} \quad \text{on the free surface,} \tag{4.13}$$

where $\kappa$ is the $O(1)$ curvature of the free surface in the $X$-$Y$ plane and $\text{Ca} = \tilde{\mu} \tilde{U}/\tilde{\gamma}$ is the capillary number, which is expected to be at least of $O(1)$.

As briefly mentioned in §4.1, we need four matching conditions from Regions II and IV to formally close the problem. Two of these will come from matching the pressure, and two from matching the flux. However, the far-field conditions in these inner regions arise from matching into the appropriate outer regions, which involves the unknown flux. Thus, determining the flux through these regions is important in formally closing the system. Solving each of the inner problems numerically yields a result for the scaled flux at each end of Region III.

As shown in figure 6, for Region IV we denote the film thicknesses in the separated regions as $h_+^b$ and $h_+^c$ for the fluid near the belt and cylinder, respectively. Then, the total flux into and out of Regions IV is

$$q_+ = U h_+^b + \Omega h_+^c, \tag{4.14}$$

and we note that the flux in Region III is related to this flux through

$$Q_c = H(x_+) q_+. \tag{4.15}$$

A similar result holds in Region II, where mass conservation again requires that the total flux is $Q_c$. We will return to this region later but first we will consider what extra information emerges from a study of Region IV.

### 4.3. *Direct numerical simulations of Region IV*

Here we describe the full numerical solution to the inner problem (4.11)–(4.13) in Region IV. Hence, we use $H$ to refer to $H(x_+)$ for notational convenience in this section. The far-field conditions in Region IV are obtained through matching with Region III, Region V, and Region VI. They are:

$$u \to 3 \left( 2q_+ - U - \Omega \right) Y (1 - Y) + (\Omega - U) Y + U, \quad V \to 0 \quad \text{as } X \to -\infty, \tag{4.16a}$$

$$u \to U, \quad V \to 0 \quad \text{as } X \to +\infty, \text{ with } Y \in (0, h_+^b) \tag{4.16b}$$

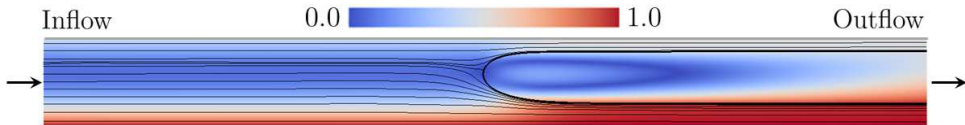$$u \to \Omega, \quad V \to 0 \quad \text{as } X \to +\infty, \text{ with } Y \in (1 - h_+^c, 1). \tag{4.16c}$$

Figure 7: Full computational domain constructed in *Basilisk*, with the background colour showing the norm of the calculated velocity field $\mathcal{U} = (u^2 + V^2)^{1/2}$ in both liquid and gas regions, and the interface separating them highlighted in a thick black line. Thin black lines are used for presenting selected streamlines inside the liquid region. This particular case study is described by parameter values Ca $= 2.0$, $U = 1.0$, and $\Omega = 0.6$. Enhanced video supplementary material expands on the setup and individual contributions of specific flow components.

We emphasise that $q_+$, $h_+^b$, and $h_+^c$ are *a priori* unknown, but linked through the conservation of flux relationship (4.14). The goal of solving this system is to determine these parameters which will, in turn, allow us to derive a closed system for the motion of the cylinder and the flow structure in Region III.

Since we may reduce the dependence of this inner problem from three dimensionless parameter groupings to two by scaling the pressure and velocity with the lower wall velocity, we henceforth take $U = 1$ without loss of generality. For given values of Ca and $\Omega$, we implement and solve a generalised version of the system formed by equations (4.11)–(4.13) and (4.16) using the open-source *Basilisk* platform (see `http://basilisk.fr/` or Popinet (2020) for details). The package provides functionality for the solution of partial differential equations using a second-order time- and space-adaptive finite volume methodology. The generalisation stems from the fact that both liquid and gas environments are accounted for in a time-dependent setting, with fictitious time introduced to allow easy and accurate iterations towards a steady state solution. The physical properties of the gas are well aligned with the asymptotic framework (hydrodynamically passive, with a density ratio of $10^{-3}$ and viscosity ratio of $10^{-2}$ relative to the reference liquid), while a small dimensionless gravitational acceleration contribution (of magnitude $10^{-2}$) is imposed in the negative $X$-direction at the level of the entire multi-fluid system, even though it will soon be apparent that gravitational effects are negligible in the nip region. Interfacial advection is performed using a conservative scheme, as described by Weymouth & Yue (2010), while the well-known continuum surface force (CSF) model by Brackbill *et al.* (1992) is employed to include surface tension effects.

At the grid level, the method lives on a quadtree structure, which ensures efficient multi-scale capabilities, as well as convenient parallelisation features, with aspects surrounding the algorithm and in particular interfacial reconstruction described by Popinet (2009). For the present investigation, the computational domain is set to occupy a region of dimensionless size $20 \times 1$ (illustrated in figure 7), which extensive testing has shown to be sufficient in allowing an accurate imposition of both inlet and far-field conditions on the basis of quantitative confirmation of converged locally parallel flows in the respective regions. The mesh adaptivity strategy is built around the location of the fluid-fluid interface, as well as changes in the magnitude of the velocity components. It retains a sufficiently large number of degrees of freedom (typically of $\mathcal{O}(10^5)$ and with a reduction of a factor of $3 - 5$ over an equivalent uniform mesh) in sensitive regions, such as for example cases with a relatively low value of $\Omega$, in which the interface may approach the upper boundary to within a distance of $\mathcal{O}(10^{-2})$. A typical convergence procedure to a steady state solution involves an adjustment of an initially prescribed interfacial
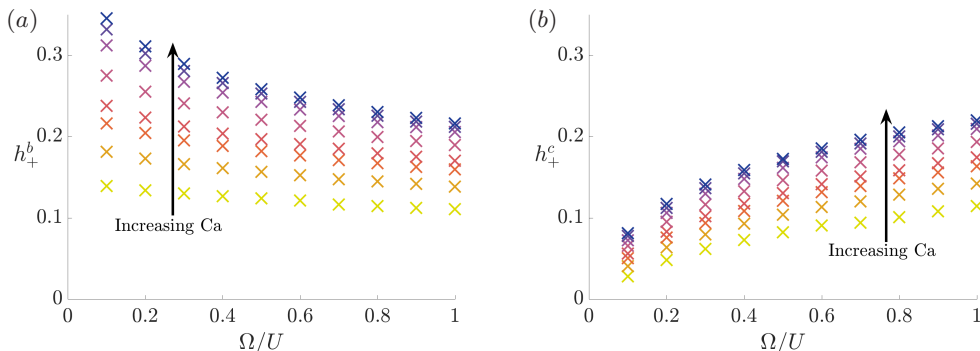
Figure 8: The key results from the DNS of the inner problem we derive in §4.2; (a) $h_+^b$, the height of the film on the belt and (b) $h_+^c$, the height of the film on the cylinder. The different colours represent different values of Ca $\in \{0.2, 0.4, 0.7, 1, 2, 5, 10, 20\}$, in the direction indicated by the arrow.

profile (formed by the union of strip regions of prescribed width joined by a semicircular tip) and the inlet condition (restricted by the functional form in (4.16a), but with $q_+$ as an additional allowed degree of freedom), such that the interfacial tip location no longer changes in time. This can be summarised as a feedback relaxation method where we slowly vary $q_+$ in response to the interface location until the free boundary stops translating in $X$. The procedure requires $\mathcal{O}(10^2)$ CPU hours for each individual run (executed in parallel, most often over 16 CPUs, on local high performance computing facilities). Video supplementary material for a particular case is provided for reference, using the parameters indicated in figure 7. The method ultimately yields values of $q_+$, $h_+^b$, and $h_+^c$ for a steady solution, for given Ca and $\Omega$.

We find that increasing Ca increases both $h_+^b$ and $h_+^c$, but this increase is bounded above as Ca becomes large (figure 8). Conversely, as Ca is decreased, $h_+^b$ and $h_+^c$ both become small. This requires a significant decrease in mesh size to resolve, which makes the simulations very computationally expensive for smaller values of Ca. Increasing $\Omega$ decreases $h_+^b$ but increases $h_+^c$, as more of the fluid shifts towards the cylinder surface. When $\Omega = 1$, we find that $h_+^b = h_+^c$, as one would expect from the symmetry of the problem. When $\Omega$ becomes small, the singular nature of the problem ($h_+^c \to 0$ in this limit) means that the simulations become much more computationally expensive, for similar reasons as for small Ca.

Strikingly, we find that the ratio of film heights is related to the ratio of boundary velocity through a two-thirds power-law. That is, we find that in all DNS the results collapse onto the following curve

$$h_+^c/h_+^b = \left(\frac{\Omega}{U}\right)^{2/3}, \qquad (4.17)$$

as shown in figure 9. This is similar to the observation in Coyle *et al.* (1986), where the authors solve a similar Region IV (separation) inner problem numerically and state that the relationship $h_+^c/h_+^b = (\Omega/U)^{0.65}$ appears to hold for Ca $> 0.1$. While the small-Ca limit is difficult to resolve numerically and is not relevant to our experiments, the power-law relationship does continue to hold in this limit, as we show in Appendix A through an asymptotic analysis.

The computational results we have presented in figure 8 provide the two remaining
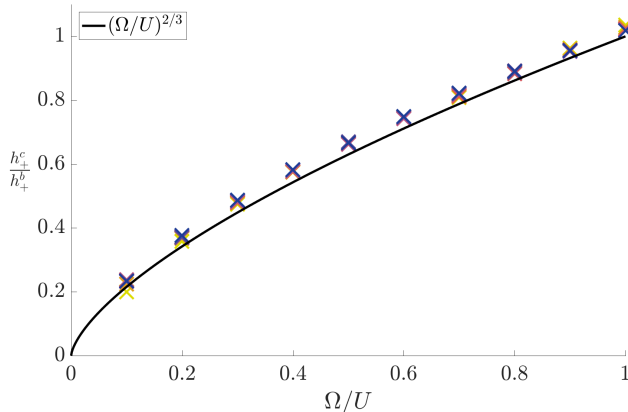
Figure 9: All DNS data from figure 8 approximately collapses onto the curve $h_+^c/h_+^b = (\Omega/U)^{2/3}$. For each value of $\Omega/U$, there are eight different individual runs that appear to have collapsed onto a single point, so there are 80 simulations represented in this figure in total. The eight values of Ca $\in \{0.2, 0.4, 0.7, 1, 2, 5, 10, 20\}$ correspond to different colours, as described in figure 8.

closure conditions required to understand the cylinder motion. In the next section, we bring together all seven equations needed to solve the problem.

### 4.4. *Closing the problem*

There are seven unknowns in the problem: $\Omega$, $Q_c$, $h_0$, $P_0$, $x_-$, $x_+$, and $U$. Of the seven equations required to determine these, three arise from the global force and torque balances (3.11)–(3.12). The leading-order contributions from these global conditions all emanate from Region III, so using the stress results from this region (4.8), and noting that $(1, \epsilon^{1/2}x)$ is tangent to the cylinder yields

$$\int_{x_-}^{x_+} p \, \mathrm{d}x = 0, \tag{4.18a}$$

$$\int_{x_-}^{x_+} xp + \left.\frac{\partial u}{\partial y}\right|_{y=H} \mathrm{d}x + M = 0, \tag{4.18b}$$

$$\int_{x_-}^{x_+} \left.\frac{\partial u}{\partial y}\right|_{y=H} \mathrm{d}x = 0. \tag{4.18c}$$

Here, (4.18a) is the force balance in the $y$-direction, (4.18b) is the force balance in the $x$-direction, and (4.18c) is the moment balance. We note that imposing (4.18c) will simplify (4.18b). A consequence of (4.18b) is the physical interpretation that the force levitating the cylinder depends on the pressure variation within the nip. This contrasts with the result for the block in Mullin *et al.* (2020) where levitation resulted from the shear forces.

Two additional equations arise from asymptotically matching the pressure in Region III with the pressure in the coalescence and separation regions II and IV. Since the pressure in Region III is asymptotically larger than the pressure in the coalescence and separation regions II and IV, as can be seen from the pressure scaling in (4.10), matching yields the conditions

$$p(x_-) = 0, \qquad p(x_+) = 0. \tag{4.18d}$$

As (4.18) only consists of five equations in total, it remains to determine two additional equations to close the system. These two degrees of freedom correspond to our current lack of information regarding the positions of the free boundaries $x_-$ and $x_+$. This is a well-studied problem in lubrication theory, see for example Coyne & Elrod Jr (1970, 1971); Ruschak (1982); Savage (1977); Stieber (1933); Swift (1932); Taroni *et al.* (2012). We note that the existence and uniqueness of solutions to the relevant inner problem remain open questions.

However, as noted above, it is possible to use two simple conditions in conjunction with our analysis in §4.2–4.3 to close the problem. Firstly, we note that both inner regions are linked through a globally conserved quantity. Due to the steady assumption, the fluid flux into Region I is the same as the fluid flux out of Region V in their respective far-fields. Hence, the film thickness is the same in these regions. In particular, this means that the fluid leaving Region IV on the belt has a dimensionless thickness of 1 in Region V. This means

$$h_+^b = 1/H(x_+), \qquad (4.19a)$$

using the scaling in (4.10). We are able to use the DNS results summarised in figure 8 to determine the left-hand side of (4.19a), and $H(x_+) = h_0 + x_+^2/2$.

Secondly, using the two-thirds power-law relationship (4.17) in conjunction with the scaled flux condition (4.14), the flux scaling (4.15), and the first closure condition (4.19a), results in the following relationship

$$Q_c = U + \Omega \left( \frac{\Omega}{U} \right)^{2/3}. \qquad (4.19b)$$

The conditions (4.19) therefore represent two independent equations to close the system in Region III. To summarise the flow of information here: solving the flow problem in Region IV yields $h_+^b$ and $h_+^c$. The former can be used in (4.19a) to obtain one closure condition. Then the power-law relationship (4.17) yields the second closure condition (4.19b). The solution will then automatically solve the equivalent Region II inner problem.

The equations (4.18) and (4.19) close the entire system, and their investigation will allow us to determine the belt speed required for balance, the rotation of the cylinder, and the flow structure in Region III. This analysis is the subject of the next section.

### 4.5. *Investigating the closed system*

In this section, we investigate the closed system we have derived, (4.18) and (4.19), to understand the critical belt speed, the motion of the cylinder, and the flow structure in Region III. Although (4.19b) is derived from DNS through (4.17), we do not require the actual DNS results to implement (4.19b). Hence, the only *explicit* appearance of the DNS results in (4.18) and (4.19) is through the left-hand side of (4.19a). Thus, to avoid errors in iterated interpolation we begin by solving the remaining six equations (4.18), (4.19b) by sweeping through different possible values of $x_+$ to generate a one-family parameter of solutions for the six remaining unknowns: $x_-$, $h_0$, $\Omega$, $P_0$, $Q_c$, and $U$, then use (4.19a) to relate $x_+$ to the experimental parameters. We also note that it is possible to scale out the mathematical dependence of the system on the parameter $M$ by solving for $\Omega/U$, $Q_c/U$, and $U/M$ instead of $\Omega$, $Q_c$, and $U$.

The resulting nonlinear algebraic system from (4.18), (4.19b) is

$$\alpha \left[ I_2 \right]_-^+ - \beta \left[ \frac{x}{H^2} \right]_-^+ = 0, \qquad (4.20a)$$
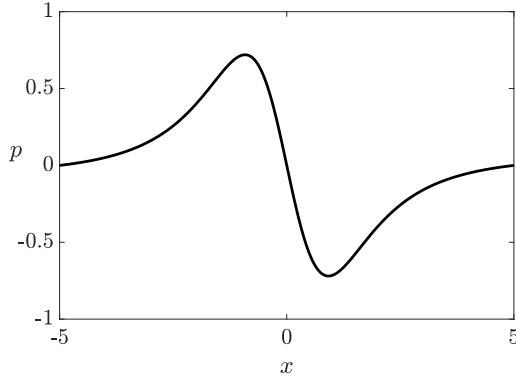
Figure 10: Typical pressure profile from (4.7), using $x_+ = 5$ to solve (4.20) yielding the solutions: $x_- = -5$, $\Omega/U = 0.282$, $h_0 = 1.33$, $M/U = 4.43$, $P_0 = 0$, and $Q_c/U = 1.12$, each correct to three significant figures.

$$P_0 + \alpha I_2(x_+) - \frac{\beta x_+}{H^2(x_+)} = 0, \qquad (4.20b)$$

$$\left(\frac{\alpha}{3} + 2\Omega\right)[I_1]_-^+ - \beta\left[\frac{x}{H}\right]_-^+ = 0, \qquad (4.20c)$$

$$\frac{\alpha}{2h_0}[xI_1]_-^+ + \beta\left[\frac{1}{H}\right]_-^+ + P_0[x]_-^+ = 0, \qquad (4.20d)$$

$$\alpha[HI_2 - I_1]_-^+ - 2h_0\beta\left[I_2 - \frac{x}{h_0 H}\right]_-^+ + \frac{P_0}{2}[x^2]_-^+ + M = 0, \qquad (4.20e)$$

$$U + \Omega\left(\frac{\Omega}{U}\right)^{2/3} - Q_c = 0. \qquad (4.20f)$$

Here, we use $[f]_-^+ := f(x_+) - f(x_-)$ for any function $f$, and introduce the following notation

$$I_1(x) := \int_0^x \frac{ds}{H(s)} \quad I_2(x) := \int_0^x \frac{ds}{H^2(s)}, \quad I_3(x) := \int_0^x \frac{ds}{H^3(s)},$$

$$\alpha = 6(U + \Omega) - 3\beta, \quad \beta = \frac{3Q_c}{h_0}, \qquad (4.21)$$

where the integrals are evaluated explicitly in Appendix B.

We note that (4.20) comprise 6 equations for 7 unknowns but, as noted above, we solve for 6 of these unknowns in terms of $x_+$ before closing the problem fully by interpolating the DNS results. We first note that $x_+ = -x_-$ and $P_0 = 0$, so $p$ must be odd in $x$. This follows from the symmetry of $p_x$ in $x$ and the fact that $p$ has only two turning points, both of which follow from (4.6), in conjunction with (4.18a) and (4.18d). A typical solution for the pressure is shown in figure 10. It is helpful to note the large-$x_+$ asymptotic solutions for the remaining variables $\Omega/U$, $h_0$, and $M/U$. We find

$$\Omega/U \sim \frac{2\sqrt{3}}{\pi x_+}, \quad h_0 \sim \frac{3}{2} - \frac{3\sqrt{3}}{\pi x_+}, \quad M/U \sim \frac{4\pi}{\sqrt{3}} - \frac{12}{x_+} \quad \text{as } x_+ \to \infty. \qquad (4.22)$$

These provide accurate initial guesses to solve the system (4.20) for large $x_+$, and then we are able to search for a solution to (4.20) with a slightly smaller $x_+$ by iterating using the previously found solution as an initial guess, all the way down to small values of $x_+$.
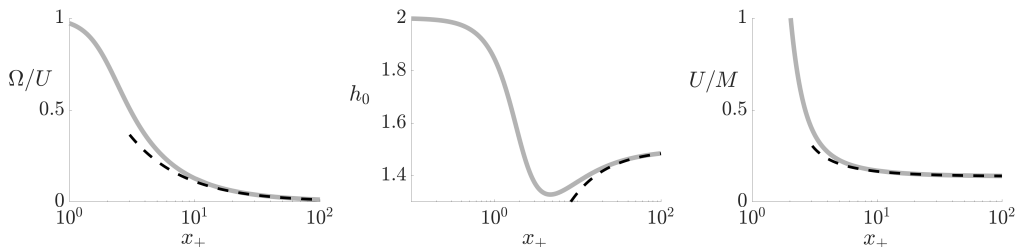
Figure 11: Solutions to the nonlinear system (4.20) as functions of $x_+$ in terms of the scaled cylinder rotation rate $\Omega/U$ (left), the nip height $h_0$ (centre), and scaled belt velocity $U/M$ (right). The solid grey line represents the numerical solution. The dashed black lines represent the large-$x_+$ asymptotic solutions (4.22).
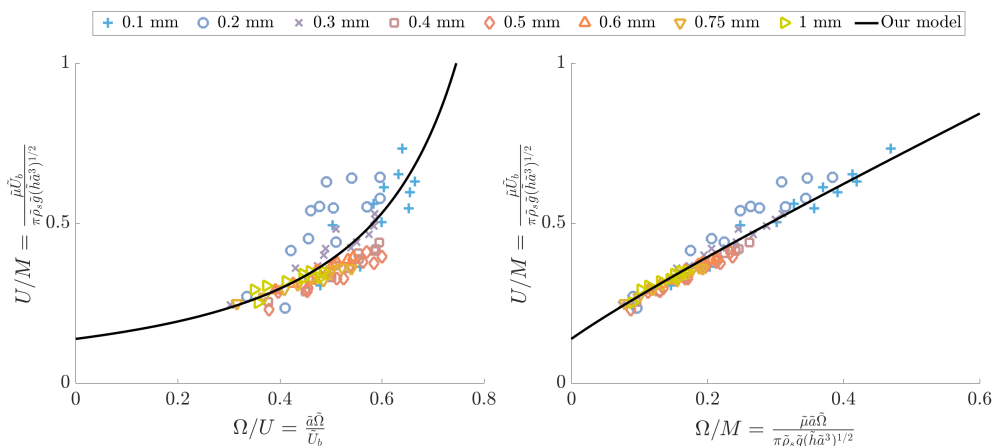


Figure 12: Comparison between the experimental data of Eggers *et al.* (2013) and our theoretical predictions in terms of the relationship between $\tilde{\Omega}$ and $\tilde{U}_b$. In (a), we present the data in the same manner as in Eggers *et al.* (2013) (with different notation), and in (b), we separate $\tilde{\Omega}$ and $\tilde{U}_b$ onto each axis. The markers correspond to the experimental data, with the legend entries corresponding to film thickness. Within each group of marker type, the cylinder radius varies.

We find that $\Omega/U$ and $U/M$ both monotonically decrease as $x_+$ increases from zero to infinity (grey lines in figure 11). However, $h_0 \in (h_{\min}, 2)$ is a non-monotonic function of $x_+$, where the minimum value $h_{\min} \approx 1.327$ occurs at $x_+ \approx 4.675$.

To validate our model, we compare our theoretical results with the experimental data from Eggers *et al.* (2013) in figure 12, where both the film thickness and the cylinder radius are varied. We are able to do this by using $x_+$ as the parameter when we plot $U/M$ and $\Omega/U$. We see good agreement between theory and data across a wide range of film thicknesses and cylinder radii. That is, the experimental data collapses onto the one-parameter family of solutions that we derive. The only data set that does not appear to collapse onto the theory curve is for a film thickness of 0.2 mm, one of the thinnest films tested, for which our model over-predicts the rotation rate. As noted in Eggers *et al.* (2013), we expect surface roughness to affect the results more for thinner films which could explain this small discrepancy. We also note from figure 12a that the largest
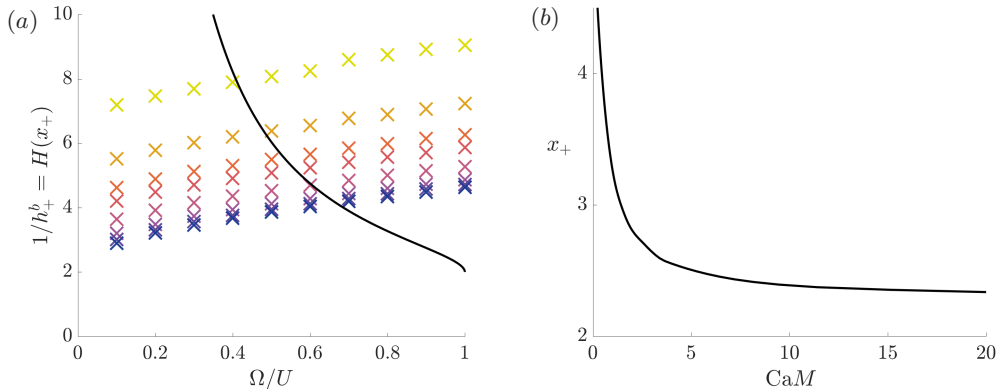
Figure 13: The closure results from DNS of the inner problem we derive in §4.2; (a) $H$, the splitting height in Region III, where the eight different colours correspond to different values of Ca $\in \{0.2, 0.4, 0.7, 1, 2, 5, 10, 20\}$ as described in figure 8, with the one-parameter family of solutions derived in §4.5 overlaid. Interpolating our DNS results along this solution curve and combining it with the results from §4.5 yields: (b) $x_+$ in terms of Ca$M$, which is specified by the experimental setup.

experimentally observed value of $\Omega/U$ is just below 0.67, as predicted by our model, which we will discuss below.

We now use (4.19$a$) to determine the full solution of the system in terms of the control parameter $M$, which is determined by the experimental setup. We do this by interpolating the DNS results from figure 8a onto the one-parameter family of solutions to (4.20) that we derive above. We show the route this one-parameter family of solutions takes through the DNS-determined $H(x_+)$ in figure 13a. We note that figure 13a predicts that $\Omega/U$ can never be larger than 0.67 (to two significant figures), which occurs at the point at which the solution branch drops below the DNS data for large Ca. Combining these DNS results with the condition (4.19$a$) provides a relationship between Ca$M$ and $x_+$ (figure 13b). In general, $x_+$ decreases as Ca$M$ increases, but this is bounded below by $x_+ \approx 2.3$, which appears to be the minimal possible value of $x_+$ for this problem. As Ca$M$ becomes small, the value of $x_+$ becomes large. This corresponds to small values of $h_+^b$ and $h_+^c$ in the DNS, which means that this limit is more difficult to resolve numerically. We will discuss this limit in more detail in §5.

The analysis above has implicitly relied on a vital constraint that must be satisfied for its validity, namely that $x_+$ is finite. When we plot the response diagram for the scaled belt speed as a function of $M$, we find that this function is nearly linear, as in figure 14a (and the same applies to the scaled rotation rate in figure 14b). In particular, we note that for the experiments in figure 3, for which $M = 2.2$, figure 14a predicts that $U = 1.4$ so that $\tilde{U}_b = 14$ mm s$^{-1}$, which is reasonable agreement with the measured value of 10 mm s$^{-1}$. The results of figure 14 provide a solution for the dimensional belt speed $\tilde{U}_b$ and rotation rate $\tilde{\Omega}$ for any given cylinder.

More importantly, from figure 13b we see that the limit $M \to 0$ results in $x_\pm \to \pm\infty$. Additionally, from figure 14, the same limit results in both $U \to 0$ and $\Omega \to 0$. In this limit of small cylinder mass our previous analysis is invalid; we now describe a scenario for the levitation of cylinders of small mass.
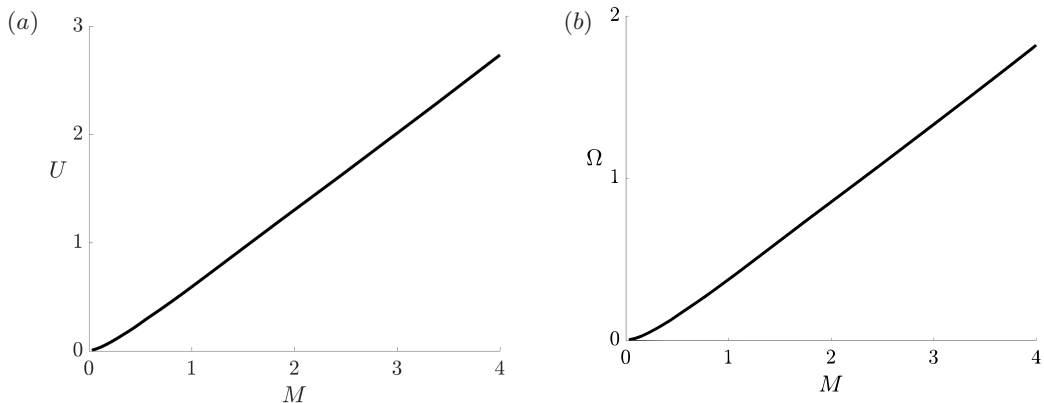
Figure 14: The dimensionless (a) belt velocity and (b) cylinder rotation rate, in terms of the dimensionless weight per unit length of the cylinder, $M$, specified by the experimental setup. We use the typical belt velocity $\tilde{U} = 10$ mm s$^{-1}$; different choices will result in differently scaled axes consistent with the definitions of the dimensionless parameters.

## 5. Levitation of light cylinders

The previous section has shown that, over a large parameter range, the dependence of levitation on the belt speed can be explained without any discussion of gravitational effects in the fluid. However, although this 'zero-gravity' scenario applies whenever the dimensionless film thickness in the nip is everywhere of $O(\epsilon)$, it needs to be revised in configurations in which the cylinder mass $M$ is small and $|x_\pm| \to \infty$, causing the the length and thickness of the lubrication layer to increase. We now describe how this involves the incorporation of gravitational effects in the lubrication regime and this will ultimately lead to an explanation for the fluid tongues shown in figure 2, for cylinders that are less dense than those modelled in §4. For definiteness, in this section we take Ca $= 1$, but note that the results hold qualitatively for Ca $= O(1)$.

### 5.1. The limit $M \to 0$ in the lubrication regime

We now consider what happens as $x_- \to -\infty$ in (3.8), recalling that $U = O(M)$ and $\Gamma = O(1)$ as $M \to 0$. The gravitational term becomes relevant when $y = O(M^{1/2}\epsilon^{-3/4})$ and, since the film thickness is of $O(x^2)$, $x = O(M^{1/4}\epsilon^{-3/8})$. As we require $x$ to be large, we will only consider cylinders whose mass is such that $M \gg \epsilon^{3/2}$. Hence, we rescale

$$x = M^{1/4}\epsilon^{-3/8}\overline{x}, \quad y = M^{1/2}\epsilon^{-3/4}\overline{y}, \quad u = M\overline{u}, \quad v = M^{1/4}\epsilon^{-3/8}\overline{v}, \quad p = M^{1/4}\epsilon^{9/8}\overline{p}, \tag{5.1}$$

which leads to a model that differs from that in the nip only in the $x$-momentum equation in (3.8), which at leading order becomes

$$\frac{\partial \overline{p}}{\partial \overline{x}} = \frac{\partial^2 u}{\partial \overline{y}^2} - \Gamma \quad \text{for } 0 < \overline{y} < \frac{\overline{x}^2}{2}. \tag{5.2}$$

The solution must match with that in the nip as $\overline{x} \to 0$ and, since the nip solution gives that $U/M \sim \sqrt{3}/4\pi$ and, from (4.22) $\Omega = O(M^{3/4}\epsilon^{3/8})$ as $M \to 0$, the boundary conditions are

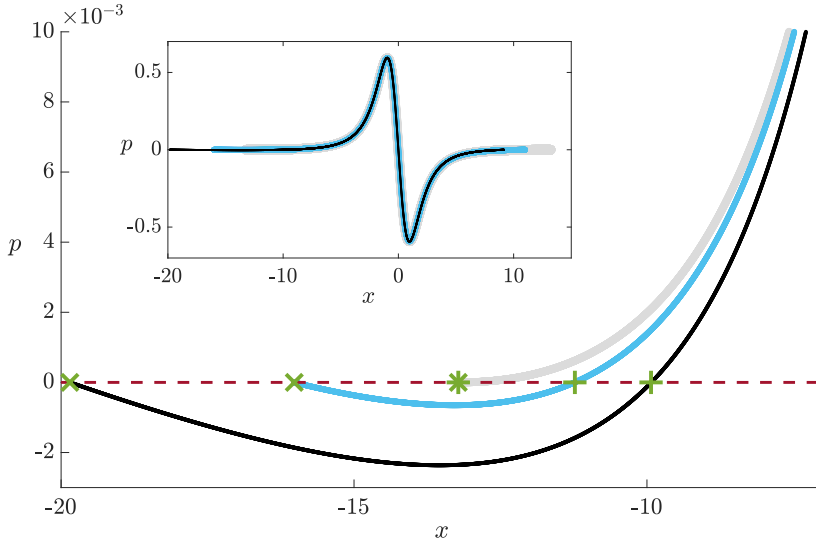$$\overline{u} = \frac{\sqrt{3}}{4\pi}, \quad \overline{v} = 0 \quad \text{on } \overline{y} = 0, \tag{5.3a}$$

Figure 15: Pressure profiles in the flooded region where $p < 0$. The solid lines show pressure profiles, for different values of $M$, and the red dashed line marks zero. The $+$ symbols mark $\overline{x}^*_-$ and the $\times$ symbols mark $\overline{x}^{\circ}_-$. For the grey line, these symbols mark the same point; this occurs when $\overline{p}_{\overline{x}}(\overline{x}^*_-) = 0$. In the inset we show the same pressure profiles over the entire domain, which reveal very little difference between profiles in the nip region - the major difference is their horizontal extent.

$$\overline{u} = 0, \quad \overline{v} = 0 \qquad \text{on } \overline{y} = \frac{\overline{x}^2}{2}. \tag{5.3b}$$

Hence, we find that

$$\overline{p} = -\Gamma \overline{x} - \frac{2\sqrt{3}}{\pi \overline{x}^3} + C, \tag{5.4}$$

for some constant $C$ that would be determined through matching with higher-order terms in the nip region.

We note that the effect of this longer lubrication region on the force and moment balance equations (4.18a)–(4.18c) is of $O(M^{-1/4}\epsilon^{3/2})$ compared to the forces exerted in the nip and hence it can be neglected to leading order. From (5.4) we see that it is now possible for the pressure to vanish at two points $\overline{x} = \overline{x}^*_-$, $\overline{x}^{\circ}_-$ in $\overline{x} < 0$, as shown in figure 15. Here, we have set the pressure to be zero when $\overline{x}$ exceeds the value $\overline{x}_+$ because there is no experimental evidence that the upper meniscus ever moves much beyond the nip region where $x = O(1)$. The response diagram for $|x_-|$ as a function of $M$ in the extended region is as in figure 16, the physically relevant branch tending to infinity as $M \to 0$, as discussed at the end of §4.

Although we do not determine the constant $C$ in (5.4), we note that the pressure minima in the flooded regions in figure 15 occur when

$$\overline{x} = \overline{x}_m := -\left(\frac{6\sqrt{3}}{\pi \Gamma}\right)^{1/4}, \tag{5.5}$$

and that $M = M^*$ in figure 16 when $\overline{p} = 0$ at this point. As $M$ decreases below $M^*$, the region under the cylinder floods more and more fluid down the belt and this suggests a
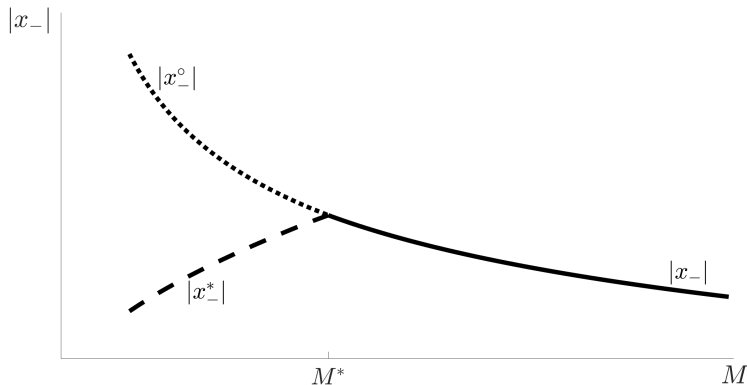
Figure 16: Schematic response diagram for the spatial positions in $\overline{x} < 0$ where the pressure vanishes. As $M$ decreases, there is a critical value at which the pressure can vanish at two upstream values. These mark the approximate start and end of the flooded region.

possible explanation for the tongues observed in figure 2. In the next section, we briefly recapitulate a simple two-dimensional theory for such tongues.

### 5.2. *Tongue modelling*

A simple model for a tongue when levitating a block has been described in Mullin *et al.* (2020). By including gravity effects into the lubrication equations, and allowing for recirculating flow, the uniform tongue thickness, $h_t$, including the fluid initially on the belt, satisfies the dimensional cubic equation

$$\tilde{U}_b \tilde{H}_t - \frac{\tilde{\rho}\tilde{g}}{3\tilde{\mu}} \tilde{H}_t^3 = \tilde{Q}, \tag{5.6}$$

where $\tilde{Q}$ is the dimensional net mass flux; for a steady tongue $\tilde{Q}$ is the mass flux past the scraper.

Following §5.1, we scale the tongue thickness by writing $\tilde{H}_t = \epsilon^{1/4} M^{1/2} \tilde{a} h_t$, so that (5.6) becomes

$$\frac{\sqrt{3}}{4\pi} h_t - \frac{\Gamma}{3} h_t^3 = O(\epsilon^{3/4}), \tag{5.7}$$

so that

$$h_t = \left(\frac{3\sqrt{3}}{4\pi\Gamma}\right)^{1/2}, \tag{5.8}$$

to lowest order. This suggests that, if a tongue exists, it will terminate at the cylinder near the point

$$\overline{x} = \overline{x}_t = -\left(\frac{12\sqrt{3}}{4\pi\Gamma}\right)^{1/4}, \tag{5.9}$$

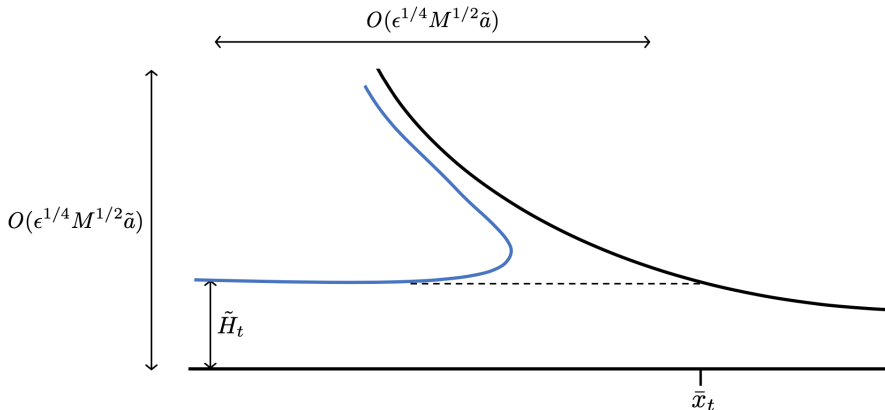which is where the upper surface of the tongue intersects the cylinder.

Figure 17: Schematic of the putative inlet coalescence region when a tongue is present.

### 5.3. *Matching the nip and tongue regions*

The discussion of §5.1 suggests that, as $M$ decreases, the flooded region below the nip will extend down to the increasingly remote point $\overline{x}^{\circ}_{-}$. In the vicinity of this point we expect a local region to occur in which a fully two-dimensional Stokes flow model is included, as in Region IV. This region will join the lubrication region in $\overline{x}^{\circ}_{-} < \overline{x}$, with the coating flow coming around the cylinder and the incoming film on the belt. However, to confirm this would require an analysis similar to that in Region IV, which we will not pursue here. A further two-dimensional model would be needed when $\overline{x}^{\circ}_{-}$ reaches $\overline{x}_t$, which is larger in modulus than the minimum pressure point given by (5.5). Then, a tongue will form and we expect a configuration as in figure 17 where the transverse lengthscale is $O(\tilde{a}\epsilon^{1/4}M^{1/2})$.

It is reassuring that, for all values of $M$, the dominant levitation forces still occur in the nip, so that our prediction that there is always a unique belt velocity for any given $M$ still holds. This is in contrast to the levitation of blocks (Mullin *et al.* 2020) where, although the force and moment balances could be satisfied without a tongue for a unique belt velocity, a continuous range of belt velocities were possible in the presence of a slowly evolving tongue.

We remark that when the cylinder is made lighter by reducing its radius rather than its density, an even more complicated asymptotic analysis becomes necessary. As mentioned in the Introduction, experimental evidence suggests that a downward propagating tongue is more likely to occur for smaller radii cylinders.

We summarise this section by listing our main predictions in the flooding regime when $M \ll 1$:

(i) The zero-gravity theory in §4 holds for $M = O(1)$ and, to lowest order, it predicts an odd pressure distribution that vanishes at $x = x_-, x_+$, as in figure 10 and figure 15 (grey line in inset). However, as $M \to 0$, $|x_\pm| \to \infty$ and, as shown in §5.1, gravitational effects become comparable with viscous effects when the dimensional nip extent in the $x$-direction is of $O(M^{1/4}\epsilon^{1/8}\tilde{a})$. As long as $\epsilon^{3/2} \ll M \ll 1$, this exceeds the nip length of $O(\epsilon^{1/2}\tilde{a})$ in Region III: the regime in which $M = O(\epsilon^{3/2})$ requires further study.

(ii) The incorporation of gravity means that the nip pressure distribution is no longer an odd function of $x$ as it was in figure 10 and figure 15 (grey line in inset). This allows flooding, in which the nip region extends downwards to the green crosses marked in figure 15. There is then an extended nip region in which gravity is included but the dominant

lubrication forces still occur in the original nip region of length $O(\epsilon^{1/2}\tilde{a})$. Hence, the prediction that the dimensionless belt velocity is $U = \sqrt{3}M/(4\pi) \ll 1$ remains valid to lowest order, and the corresponding dimensional value is $\tilde{U}_b \sim (3\tilde{h}\tilde{a}^3)^{1/2}\tilde{\rho}_s\tilde{g}/4\tilde{\mu}$.

(iii) A more precise estimate of the dependence of the length of the flooded region on $M$ can be obtained from the dependence of $x_\pm$ on $M$. Since scaling the velocity and pressure in Region IV with $U \ll 1$ in §4.2 leads to the same problem except with an effective capillary number of $U\mathrm{Ca}$, the results of Appendix A allow us to deduce that $M = O(U) = O((h_+^b)^{3/2}) = O(|x_-|^{-3})$ in the limit of small $M$, which is consistent with figure 13b. Thus, $M$ is correlated to $\epsilon$ by $M \sim M^{-3/4}\epsilon^{9/8}$, *i.e.* $M \sim \epsilon^{9/14}$. This gives the dimensional extent of the flooded region to be of $O(\epsilon^{2/7}\tilde{a})$, and the dimensional angular velocity to be of $\tilde{\Omega} = O(\epsilon^{3/14}\tilde{U}_b/\tilde{a})$.

(iv) All the above comments apply when Ca is $O(1)$, but if the surface tension is sufficiently small so that $\mathrm{Ca}M$ is large, then $x_-$ will remain finite and no flooding will occur.

## 6. Discussion

We have investigated the levitation of a rigid cylinder placed on a thin viscous film on the surface of a belt that moves vertically upwards. Using a combination of asymptotic analysis and direct numerical simulation, we have found that the configuration of the lubrication region that levitates the cylinder changes markedly for cylinders of different mass. However, in all cases, the dominant levitation forces occur in the nip region where the cylinder is closest to the belt, and gravity forces in the fluid are negligible in this region.

We have found that there is a unique belt speed that allows levitation, for any given cylinder mass and radius. This speed, and the rotation rate of the cylinder about its own axis, decrease as the cylinder mass decreases. Our theoretical predictions agreed with the experimental data reported in Eggers *et al.* (2013). For sufficiently light cylinders, gravity in the fluid is important in the lower part of the lubrication region, and this can lead to tongue formation on the belt beneath the cylinder.

It is interesting to compare our predictions concerning the dependence of tongue evolution on the dimensionless weight per unit length of the cylinder, $M$, with the experimental evidence shown in figure 18. This shows that levitated solid cylinders of different radii exhibit faster tongue growth rates as the radius decreases. For the particular experimental setup and cylinder sizes used in figure 18, the tongue does not grow when the cylinder diameter is 7.95 mm or larger, and the tongue reaches the oil supply bath when the cylinder diameter is 6.5 mm or smaller. The long-time length of the tongue saturates for intermediate diameters. The results shown here are typical for a wide range of film thicknesses, with saturation of the length of the tongue occurring over narrow ranges of diameter for thinner layers. Since the cylinder radius affects several key dimensionless parameters, a mathematical analysis involving the radius as a control parameter (rather than the cylinder density used in the definition of $M$) would be significantly more involved. Adapting our model to explore the effect of different cylinder radii on the time-evolution of the tongue remains a topic for future research.

Our theory relies heavily on the behaviour of the fluid in the region where the lubricating film in the nip splits into two films attached to the cylinder and belt. In this region, the free boundary of the fluid may have a small enough radius of curvature for capillarity to be important and there is a long history of such slow-flow free boundary problems. Even without capillarity, the mathematical well-posedness of the inner problem remains an open question. Here, we solved the inner problem using direct numerical
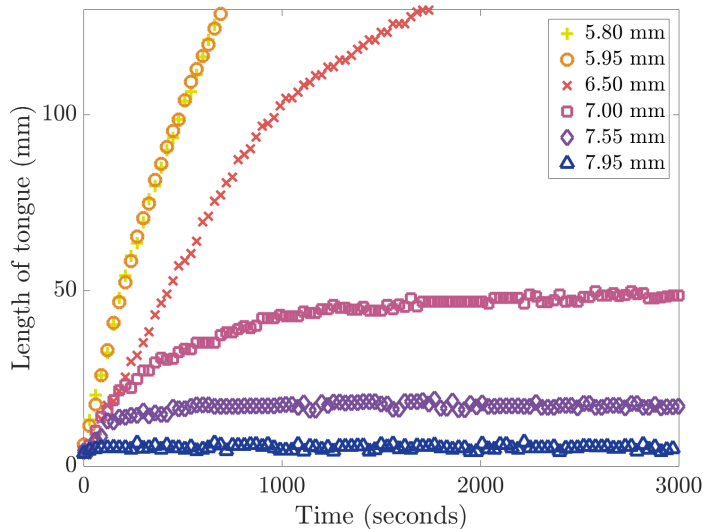
Figure 18: The evolving tongue length over time for printed plastic (ABS) cylinders of length 12.35 mm and diameter 5.80, 5.95, 6.50, 7.00, 7.55 and 7.95 mm, as labelled in the legend. The available length of the belt above the bath of oil was approximately 140mm. The upstream fluid thickness was set at 0.8 mm, and images of the tongue were taken at one second intervals using a Nikon digital SLR camera with a 50 mm close-up lens. Errors in the estimates of the length were at the level of a pixel and are hence at the level of the symbols used in the figure.

simulations on the full problem in the inner region for a wide range of parameter values. This procedure gives solutions to the large-time limit of an evolving two-phase flow in which motion of the air is taken into account, as well as capillarity. This bypasses any indeterminacy that may occur in the derived inner steady-state problem, which still poses serious mathematical challenges.

In contrast to the case of a levitating block (Mullin *et al.* 2020), where the dominant lifting force is fluid shear, we find that the dominant lifting force for cylinder levitation is the pressure difference within the nip region acting vertically on the cylinder surface. Balancing this with the gravitational force provides a simple scaling argument for the belt speed required for levitation. The appropriate pressure scale in the nip region is $\tilde{\mu}\tilde{U}_b\tilde{a}^{1/2}/\tilde{h}^{3/2}$, and the horizontal extent of the cylinder surface that can be acted upon vertically is $\tilde{h}$. Combining these and balancing with the cylinder weight per unit length $\tilde{\rho}_s\tilde{g}\tilde{a}^2$ yields the belt velocity scaling $\tilde{U}_b = O(\tilde{\rho}_s\tilde{g}(\tilde{h}\tilde{a}^3)^{1/2}/\tilde{\mu})$, and the precise value of $\tilde{U}_b$ can be read off from figure 14a.

We note that our model could be adapted to consider the problem of a cylinder rolling down a coated inclined plane. However, equation (4.18a) would contain an extra term and this would require the calculation of squeeze film forces in the nip. Hence the relation between $U$ and $M$ at the onset of flooding and tongue formation would be different.

## Acknowledgements

of the experiment. Some of the experiments were performed in the Observatory in the Mathematical Institute and the authors are grateful to Dominic Vella for providing laboratory space.

## Declaration of Interests

The authors report no conflict of interest.

## Appendix A. Asymptotic analysis of Region IV when $\mathrm{Ca} \ll 1$

In the small-Ca limit, Region IV splits into five further asymptotic regions. In the first sub-region, the free surface is capillary static to leading-order, resulting in a semi-circle of radius $1/2$ which meets the belt and cylinder at a tangent. The fluid dragged out by the belt and cylinder is thus asymptotically small. The next two sub-regions are the small transition regions where the free surface first comes close to the belt and cylinder surfaces, respectively, and these sub-regions have thickness of $O(\mathrm{Ca}^{2/3})$ and width of $O(\mathrm{Ca}^{1/3})$, centred around the apparent touchdown point in the outer problem. In each of these sub-regions, the Landau–Levich ODE holds (Landau & Levich 1988; Levich & Landau 1942), which can be solved numerically. The final two sub-regions are long thin fluid regions of (different) constant thickness, along the belt and cylinder surfaces, respectively. These thicknesses are $h_+^b \sim A\mathrm{Ca}^{2/3}U^{2/3}$ and $h_+^c \sim A\mathrm{Ca}^{2/3}\Omega^{2/3}$, where $A \approx 0.669$ arises from solving the Landau–Levich ODE numerically. Hence, $h_+^c/h_+^b = (\Omega/U)^{2/3}$ as $\mathrm{Ca} \to 0$.

## Appendix B. Evaluating integrals in (4.21)

The integrals in (4.21) can be evaluated exactly, as follows:

$$I_1(x) := \int_0^x \frac{\mathrm{d}s}{H(s)} = \sqrt{\frac{2}{h_0}} \tan^{-1} \frac{x}{\sqrt{2h_0}}, \qquad (\mathrm{B}\,1a)$$

$$I_2(x) := \int_0^x \frac{\mathrm{d}s}{H^2(s)} = \frac{1}{2h_0} \left( \sqrt{\frac{2}{h_0}} \tan^{-1} \frac{x}{\sqrt{2h_0}} + \frac{x}{H(x)} \right), \qquad (\mathrm{B}\,1b)$$

$$I_3(x) := \int_0^x \frac{\mathrm{d}s}{H^3(s)} = \frac{3}{8h_0^2} \left( \sqrt{\frac{2}{h_0}} \tan^{-1} \frac{x}{\sqrt{2h_0}} + \frac{2h_0 x}{3H^2(x)} + \frac{x}{H(x)} \right). \qquad (\mathrm{B}\,1c)$$

### REFERENCES

BICO, J, ASHMORE-CHAKRABARTY, J, McKINLEY, GH & STONE, HOWARD A 2009 Rolling stones: The motion of a sphere down an inclined plane coated with a thin liquid film. *Phys Fluids* **21** (8), 082103.

BRACKBILL, JU, KOTHE, DB & ZEMACH, C 1992 A continuum method for modeling surface tension. *J Comp Phys* **100** (2), 335 – 354.

COYLE, DJ, MACOSKO, CW & SCRIVEN, LE 1986 Film-splitting flows in forward roll coating. *J Fluid Mech* **171**, 183–207.

COYNE, J C & ELROD JR, H G 1970 Conditions for the rupture of a lubricating film. Part i: theoretical model. *J Lubric Tech* **92**, 451–456.

COYNE, J C & ELROD JR, H G 1971 Conditions for the rupture of a lubricating film?Part II: New boundary conditions for Reynolds equation. *J Lubric Tech* **93**, 156–167.

DUFFY, BR & WILSON, SK 1999 Thin-film and curtain flows on the outside of a rotating horizontal cylinder. *J Fluid Mech* **394**, 29–49.

EGGERS, J, KERSWELL, R R & MULLIN, T 2013 Balancing a cylinder on a thin vertical layer of viscous fluid. *Physical Review E* **87** (6), 065001.

FITT, AD, KOZYREFF, G & OCKENDON, JR 2004 Inertial levitation. *J Fluid Mech* **508**, 165–174.

HINCH, EJ & LEMAITRE, J 1994 The effect of viscosity on the height of disks floating above an air table. *J Fluid Mech* **273**, 313–322.

LANDAU, L & LEVICH, B 1988 Dragging of a liquid by a moving plate. In *Dynamics of Curved Fronts*, pp. 141–153. Elsevier Inc.

LEVICH, B & LANDAU, L 1942 Dragging of a liquid by a moving plate. *Acta Physicochim. URSS* **17**, 42–54.

LHUISSIER, H, TAGAWA, Y, TRAN, T & SUN, C 2013 Levitation of a drop over a moving surface. *J Fluid Mech* **733**, R4.

DE MALEPRADE, H, SOTO, D, QUÉRÉ, D, HINCH, EJ, BAIER, T, SCHÜR, MT & HARDT, S 2018 Air-propelled, herringbone-textured platelets. *Phys Rev Fluids* **3** (10), 104101.

MULLIN, T, OCKENDON, H & OCKENDON, JR 2020 Levitation by thin viscous layers. *J Fluid Mech* **888**.

PEARSON, JRA 1960 The instability of uniform viscous flow under rollers and spreaders. *J Fluid Mech* **7** (4), 481–500.

POPINET, S 2009 An accurate adaptive solver for surface-tension-driven interfacial flows. *J Comp Phys* **228** (16), 5838 – 5866.

POPINET, S 2020 Basilisk flow solver and PDE library. `http://basilisk.fr/`, accessed: 2020-04-21.

RUSCHAK, KJ 1982 Boundary conditions at a liquid/air interface in lubrication flows. *J Fluid Mech* **119**, 107–120.

RUSCHAK, KJ 1985 Coating flows. *Annu Rev Fluid Mech* **17** (1), 65–89.

SAVAGE, M D 1977 Cavitation in lubrication. Part 1. On boundary conditions and cavity – fluid interfaces. *J Fluid Mech* **80** (4), 743–755.

SAWAGUCHI, E, MATSUDA, A, HAMA, K, SAITO, M & TAGAWA, Y 2019 Droplet levitation over a moving wall with a steady air film. *J Fluid Mech* **862**, 261–282.

STIEBER, W 1933 *Des Schwimmlager: hydrodinamische Theorie des Gleitlagers*. VDI-Verlag, GmbH.

SWIFT, H W 1932 The stability of lubricating films in journal bearings. In *Minutes of the Proceedings of the Institution of Civil Engineers*, , vol. 233, pp. 267–288. Thomas Telford-ICE Virtual Library.

TARONI, M, BREWARD, C J W, HOWELL, P D & OLIVER, J M 2012 Boundary conditions for free surface inlet and outlet problems. *J Fluid Mech* **708**, 100–110.

WEINSTEIN, SJ & RUSCHAK, KJ 2004 Coating flows. *Annu Rev Fluid Mech* **36**, 29–53.

WEYMOUTH, GD & YUE, DKP 2010 Conservative Volume-of-Fluid method for free-surface simulations on Cartesian-grids. *J Comp Phys* **229** (8), 2853 – 2865.